Asociación Argentina
de Mecánica Computacional

Mecánica Computacional Vol XXIX, págs. 8355-8374 (artículo completo)
Eduardo Dvorkin, Marcela Goldschmit, Mario Storti (Eds.)
Buenos Aires, Argentina, 15-18 Noviembre 2010

WEIGHTED POTENTIAL METHODOLOGY FOR MIXED MODE COHESIVE LAWS

Kent E. Salomonsson, Tobias J. Andersson

Mechanics of Materials, University of Skövde, Skövde, Sweden, http://www.his.se/mechmat

Keywords: Adhesive layer, Cohesive law, Fracture, Mixed-mode.

Abstract. A weighted potential methodology is developed by utilizing pure mode I and mode II energy release rate experiments to determine the traction-separation relations for thin adhesive layers. The experimentally measured energy release rates act as boundary conditions for developing a weighted potential function. Thus, the tractions for any mixed mode loading can be established. Changes of mode mix during an experiment can also be captured by the law since every mixed mode variation is given by the potential function. Furthermore, by use of an inverse J-integral approach and damage type variables, the traction-separation relations for any mode mix can be approximated by use of pure mode experiments. Numerical simulations show the applicability of the methodology. The results indicate that the methodology is promising when simulating the constitutive behavior of adhesive layers.

1 INTRODUCTION

For quite some time cohesive zone models have been developed in order to describe fracture of interfaces and delamination of layered materials. These models are intended to be used when linear elastic fracture mechanics (LEFM) is not applicable and especially for problems with large process zones. Cohesive zone models are also very attractive from a computational point of view and are implemented in most commercial finite element codes of today.

In order to determine the strength of an adhesively bonded structure it is essential to establish the constitutive behavior of the adhesive, i.e. the cohesive law of the adhesive layer during mixed-mode loading. For adhesive layers, the cohesive law describes the through-thickness behavior of the layer, and both elastic and inelastic processes such as plasticity and damage are parts of it. For thin adhesive layers, the normal mode with separation w (mode-I) and the shear or tangential mode with separation v (mode-II) shown in Fig. 1, govern the behavior, cf. Klarbring (1991).

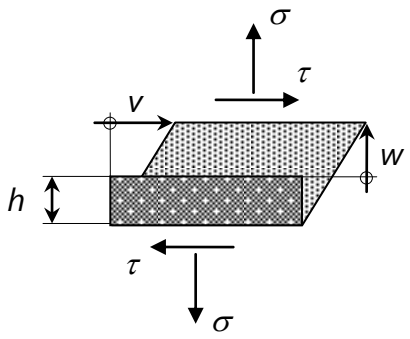

Figure 1. Normal- and tangential deformation modes of an adhesive layer.

Mixed-mode cohesive laws are commonly described by the normal and tangential tractions $\sigma(w,v)$ and $\tau(w,v)$, see Fig. 2. The shaded areas under the curves in Fig. 2 represent the accumulated energy release rates in each pure mode and the total area under each curve in each mode is the fracture energy denoted herein as Γ_{Ic} and Γ_{IIc} respectively. It can be observed in Fig. 2 that there is considerable difference between the fracture energies of the two modes. The fracture energy in mode-II, in this case, is three times larger than in mode-I. This is a common experimental observation for structural adhesives.

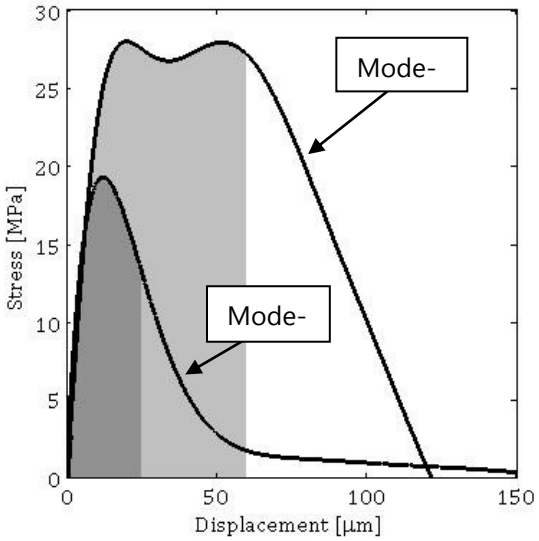

Figure 2. Experimental results with the adhesive DOW Betamate XW-1044-3.

Different approaches exist in the literature to represent the experimental behavior of structural adhesives in particular. Common employed mixed mode cohesive laws are: (i) the sawtooth-model or bilinear model (e.g. Alfano and Crisfield (2001); Högberg (2006)), (ii) the trapezoidal EPZ-model by Tvergaard and Hutchinson (1992), (e.g. Salomonsson and Andersson (2008); De Moura et al. (2008)), (iii) the exponential cohesive law by Xu and Needleman (1993), (e.g. van den Bosch et al. (2006); and (iv) the polynomial cohesive law e.g. Freed and Bank-Sills (2008) and Park et al. (2009)).

The EPZ-model developed by Tvergaard and Hutchinson (1992), is an extension of the sawtooth-model law by introducing an additional shape parameter. It is based on a potential that governs the tractions. Several experimental studies have shown that the fracture energy is dependent on the mode-mixity, e.g. Benzeggagh and Kenane (1996); Sørensen et al. (2006); Högberg et al. (2007). The exponential law introduced by Xu and Needleman (1993), is a smooth law that avoids discontinuities and thus provides an attractive choice from the computational point of view. The cohesive law introduced by van den Bosch et al. (2006), is an improved description of the exponential Xu and Needleman cohesive law. This law does not have a potential function and thus deviates from the Xu and Needleman law. However, it appears to provide a realistic mixed-mode loading behavior; which is crucial when modeling fracture of adhesive layers. A generalized potential-based cohesive law intended for mixed-mode fracture has been proposed by Park et al. (2009). This law is expressed by the use a polynomial and can therefore capture rather complex curve shapes of the normal and tangential tractions.

Cohesive models can be coupled or uncoupled. In an uncoupled model the energy release rate in one mode is independent of the separation in the other mode. Most models are however coupled e.g. Tvergaard and Hutchinson (1992). To this end, from a physical point of view a coupled model is preferred.

The literature on pure mode experiments on adhesive joints is extensive. Frequently used experimental set-ups to study mode-I and mode-II deformations are the double cantilever beam (DCB) and the end-notched flexure (ENF). The studies by Högberg (2006), and Sørensen et al. (2006), aim at presenting a method to extract mixed-mode cohesive laws that are suitable for numerical simulations. Högberg et al. (2007), have performed experiments on a so-called mixed-mode double cantilever beam, referred to as the MCB-specimen. The experimental procedure is based on the path-independence of the J-integral. The experiments reveal that the mode-mixity changes during loading towards mode-I even in the case of initial pure mode-II. Similar results are observed by Xie et al. (2005). It seems difficult to maintain a specific mode-mix experimentally. Although the cohesive law adopted in Högberg et al. (2007), considers different fracture energies in mixed-mode loading, the adopted sawtooth-model was not able to be fitted to the experimental results. This suggests that the shape of the cohesive law is of importance in mixed-mode loading. This is in accordance with observation made by e.g. Volokh (2004), and Alfano (2006). A different experimental approach has been proposed by Lundsgaard-Larsen et al. (2008). They utilize a DCB-specimen loaded with uneven bending moments to determine the cohesive law. The experimental analysis is based on a similar J-integral approach as the one used by Högberg et al. (2007).

Though it is necessary to incorporate different cohesive behaviors i.e. fracture energy and strength, in mode-I and mode-II, it is also important to consider the shape of the traction-separation relations. For example, if a saw-tooth cohesive law is chosen to model the cohesive behavior, it is difficult to capture both mode-I and mode-II curves since the shape of them can deviate significantly. For example, the normal stress curve can be similar in shape to a saw-tooth, but the shape of the tangential stress curve might be similar in shape to a trapezoidal curve. Thus, a mixed-mode cohesive law that is able to capture dissimilar cohesive behaviors plus the ability to have different shapes of the traction-separation curves in modes I and II is needed.

In this study, the intention is to develop a methodology for the development of coupled mixed-mode cohesive laws to describe mixed-mode behavior of adhesive layers that can capture the aforementioned properties. Data from pure mode-I and mode-II experiments act as input and these data can be obtained experimentally.

The paper is organized as follows. In the first section, the theoretical framework is presented. This section is followed by numerical examples to show the applicability of the mixed-mode cohesive law. Some conclusions and discussions are given in the final section.

2 THEORY

2.1 The weighted potential methodology

As a starting point, we review some of the basics of the J-integral approach to

obtain the traction-separation relations in pure mode-I and pure mode-II, cf. Sørensen and Jacobsen (2003); Alfredsson (2004); Andersson and Stigh (2004).

The external energy release rate, J_{load}, is measured experimentally for both pure mode-I and pure mode-II. To achieve an energy balance for a specific specimen, the sum of the internal energy release rate for the adhesive layer, J_{internal} and J_{load} should equal zero, i.e.

$$J_{\text{load}} + J_{\text{internal}} = 0 \tag{1}$$

Here $J_{\text{internal}} = \int_0^w \sigma(\tilde{w})\mathrm{d}\tilde{w}$ or $J_{\text{internal}} = \int_0^v \tau(\tilde{v})\mathrm{d}\tilde{v}$ depending on the pure mode. From the equality, the normal and tangential stresses are obtained by differentiation of J_{load} with respect to each relative separation, w and v.

In the present paper, the energy release rates in pure mode-I and pure mode-II are denoted, $\Gamma_{\text{I}}(w)$ and $\Gamma_{\text{II}}(v)$. These are obtained from the stresses according to

$$\begin{aligned} \Gamma_{\text{I}}(w) &= \Gamma_{\text{I}}(w,0) = \int_0^w \sigma(\tilde{w},0)\mathrm{d}\tilde{w}, \\ \Gamma_{\text{II}}(v) &= \Gamma_{\text{II}}(0,v) = \int_0^v \tau(0,\tilde{v})\mathrm{d}\tilde{v}. \end{aligned} \tag{2}$$

With $\Gamma_{\text{I}}(w)$ and $\Gamma_{\text{II}}(v)$ at hand, some essential definitions need to be established. Utilizing a polar coordinate system with an effective separation being the radius and a mode-mixity being the angle, the mode-mixity, φ, and the effective separation, λ, are defined as

$$\begin{aligned} \varphi &= \operatorname{atan}\left(\frac{w_c v}{v_c w}\right), \\ \lambda &= \sqrt{\left(\frac{w}{w_c}\right)^2 + \left(\frac{v}{v_c}\right)^2}. \end{aligned} \tag{3}$$

where, w_{c} and v_{c} are the critical normal and tangential separations in pure modes. The normal and tangential separations, w/w_{c} and v/v_{c}, are defined as the projections of the effective separation on each respective pure mode axis, see Fig. 3.

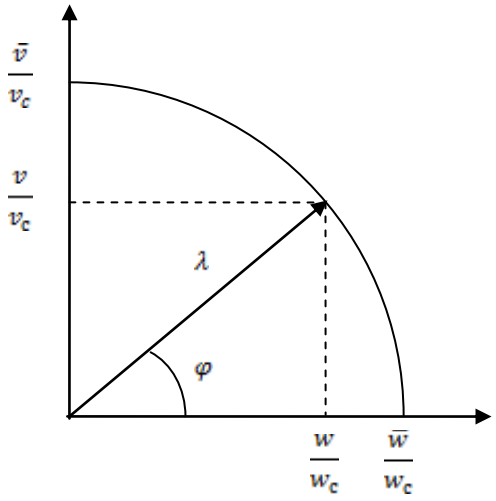

Figure 3. Illustration of effective separation and mode-mixity.

It then follows that w and v are given by

$$\begin{aligned} w &= \lambda w_c \cos\varphi, \\ v &= \lambda v_c \sin\varphi. \end{aligned} \tag{4}$$

Additional definitions, $\bar{w}$ and $\bar{v}$, are introduced as an aid of obtaining the complete, i.e. not the projected, contribution of the pure mode energy release rates to the total energy release rate. This is obtained using only λ and not the mode mixity, φ, see Fig. 3.

$$\begin{aligned} \bar{w} &= \lambda w_c, \\ \bar{v} &= \lambda v_c. \end{aligned} \tag{5}$$

As a first step in the development of the cohesive law, two independent functions can be fitted to the experimentally measured energy release rate curves, see Γ_{I} and Γ_{II} in Fig. 4.

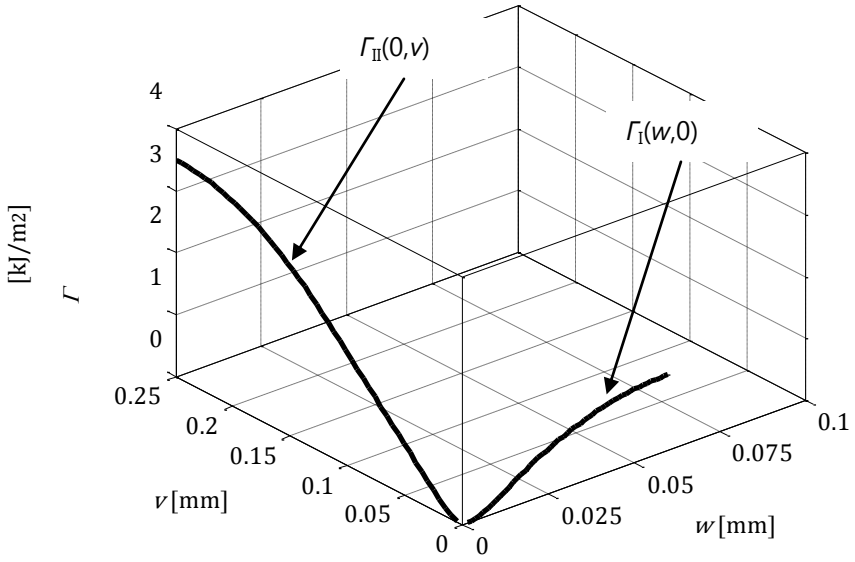

Figure 4. Fitted energy release rate curves in mode-I and mode-II.

The fitted curves are differentiated with respect to each pure mode relative separation, *w* and *v*, to establish the shapes of the traction-separation curves. Based on these curves, two laws suitable of capturing the most essential features of the differentiated curves are chosen. Figure 5 shows two idealized schematic curves.

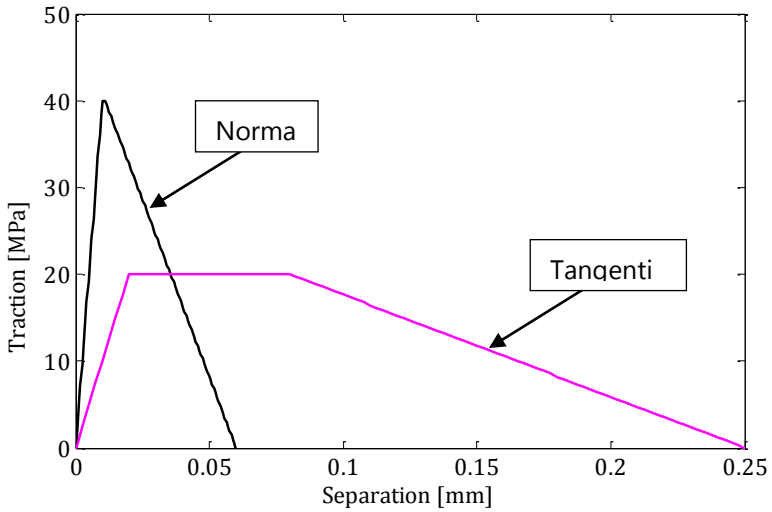

Figure 5. Schematic illustration of normal and tangential stress curves.

Now, using the Γ_I and Γ_{II} curves in Fig. 4, a surface can be constructed in a space where the axes are total energy release rate, Γ, relative normal and relative tangential separations, *w* and *v* respectively, see Fig. 6.

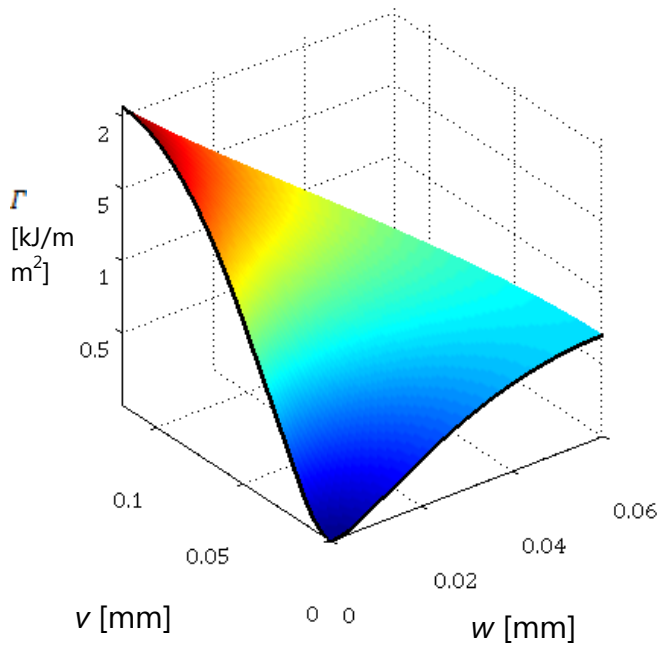

Figure 6. Weighted potential surface.

The surface, $\Gamma(\lambda,\varphi)$, representing the weighted potential, is generated by a weighted sum of the experimentally determined energy release rates in pure mode-I, $\Gamma_{\mathrm{I}}(\lambda)$, and pure mode-II, $\Gamma_{\mathrm{II}}(\lambda)$ according to

$$\Gamma(\lambda,\varphi) = f(\varphi)\Gamma_{\mathrm{I}}(\lambda)w_c^{\,2} + (1-f(\varphi))\Gamma_{\mathrm{II}}(\lambda)v_c^{\,2} = \frac{1}{2}k\lambda^2 \tag{6}$$

where $f(\varphi)$ is the weight function (or shape function). The functions $\Gamma_{\mathrm{I}}(\lambda)$ and $\Gamma_{\mathrm{II}}(\lambda)$ are obtained from experiments. The weighted potential at any given point $(\varphi\ ,\lambda)$ is assumed to correspond with an energy given by the right hand side of Eq. 6, where k is a stiffness given by

$$k(\varphi) = f(\varphi)k_1 + (1-f(\varphi))k_2. \tag{7}$$

Here, k_1 and k_2 correspond to the initial elastic stiffness in each respective mode. The normal and tangential stresses for any given mode-mix are given by partial differentiation of Γ with respect to each relative separation, w and v, respectively.

$$\begin{aligned}\sigma(w,v) &= \frac{\partial\Gamma}{\partial w} = \frac{\partial\Gamma}{\partial\lambda}\frac{\partial\lambda}{\partial w} + \frac{\partial\Gamma}{\partial\varphi}\frac{\partial\varphi}{\partial w},\\ \tau(w,v) &= \frac{\partial\Gamma}{\partial v} = \frac{\partial\Gamma}{\partial\lambda}\frac{\partial\lambda}{\partial v} + \frac{\partial\Gamma}{\partial\varphi}\frac{\partial\varphi}{\partial v}.\end{aligned} \tag{8}$$

Damage typed variables, ω_1 and ω_2, are introduced by enforcing the following

$$t_\lambda \equiv \frac{\partial \Gamma}{\partial \lambda} = f(\varphi)\frac{\partial \Gamma_{\mathrm{I}}(\lambda)}{\partial \lambda} w_c^{\,2} + (1-f(\varphi))\frac{\partial \Gamma_{\mathrm{II}}(\lambda)}{\partial \lambda} v_c^{\,2} = (1-\omega_1)k\lambda,$$
$$t_\varphi \equiv \frac{\partial \Gamma}{\partial \varphi} = \frac{\partial f(\varphi)}{\partial \varphi}\left(\Gamma_{\mathrm{I}}(\lambda) w_c^{\,2} - \Gamma_{\mathrm{II}}(\lambda) v_c^{\,2}\right) = \frac{1}{2}(1-\omega_2)\frac{\partial k}{\partial \varphi}\lambda^2. \tag{9}$$

By a simple rearrangement of Eq. 9, ω_1 and ω_2 can be determined explicitly by

$$\omega_1 = 1 - \frac{f(\varphi)\sigma(\lambda) w_c^{\,2} + (1-f(\varphi))\tau(\lambda) v_c^{\,2}}{k\lambda},$$
$$\omega_2 = 1 - \frac{2\left(\Gamma_{\mathrm{I}}(\lambda) w_c^{\,2} - \Gamma_{\mathrm{II}}(\lambda) v_c^{\,2}\right)}{\lambda^2 (k_1 - k_2)}. \tag{10}$$

2.2 Influence of $f(\varphi)$ on the traction surfaces

Next, attention is turned to the choice of the weight function, $f(\varphi)$. The choice of this function is not arbitrary. A number of conditions need to be fulfilled. By symmetry considerations the tractions must fulfill

$$\sigma(w, v) = \sigma(w, -v),$$
$$\tau(w, v) = -\tau(w, -v), \tag{11}$$

i.e. $\sigma(w,v)$ is an even function in v and $\tau(w,v)$ is an odd function of v. As a consequence of Eq. (11), a dual condition may be written as $\partial\Gamma(\lambda,0)/\partial\varphi = 0$ or $\partial f(\varphi)/\partial\varphi = 0$ according to eq. (10). Thus, the weight function $f(\varphi)$ must be an even function.

The influence of $f(\varphi)$ on the fracture energy is illustrated in Fig. 7 where the fracture energy is shown as a function of the mode-mixity for two different choices of $f(\varphi)$. It is clear that $f(\varphi)$ governs the fracture criteria. As mentioned previously the fracture energy varies with mode-mix. Thus, if Γ_c values are known from experimental mode-mix data, it is possible choose $f(\varphi)$ to fit the data. It should be noted that even though Fig. 7 shows the fracture energy as a function of mode-mixity, it is possible to use mode-mix data that might change during an experiment. These data are extracted prior to fracture and are in addition to the aforementioned pure mode experimental data.

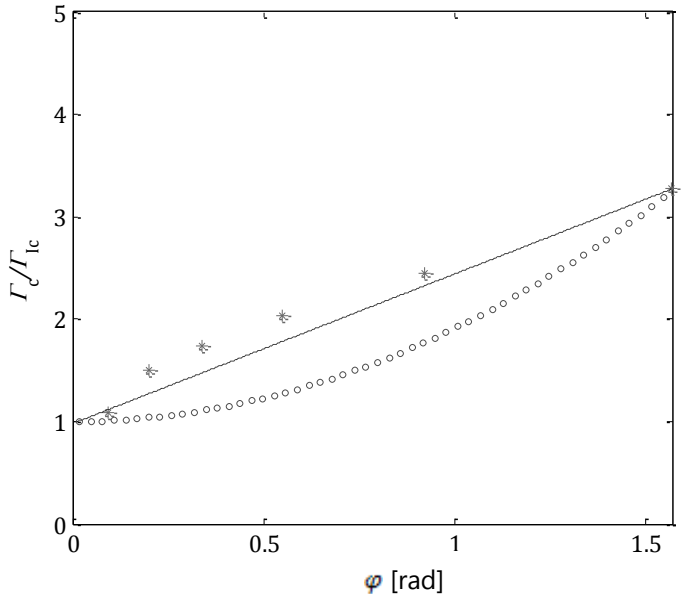

Figure 7. Γ_c/Γ_{Ic} plotted as functions of the mode-mix angle φ. The star-marked curve indicates fictitious experimental data. The dashed and the circle-marked curves indicate two choices of $f(\varphi)$ acting as approximations.

The circle-marked curve in Fig. 7 is defined as

$$f(\varphi)=1-\left(\frac{2}{\pi}\varphi\right)^2, \qquad -\frac{\pi}{2}\le\varphi\le\frac{\pi}{2} \tag{12}$$

By trying to fit a function $f(\varphi)$ to the fictitious experimental data, a linear function seems straightforward. However, $f(\varphi)$ must be an even function. To achieve this, a quadratic function in φ is used close to $\varphi = 0$ together with $|\varphi|$ according to

$$f(\varphi)=\begin{cases}1-\alpha\varphi^2, & -\varphi_1\le\varphi\le\varphi_1\\ 1-\dfrac{2}{\pi}|\varphi|, & \begin{cases}-\dfrac{\pi}{2}\le\varphi\le\varphi_1\\ \varphi_1\le\varphi\le\dfrac{\pi}{2}\end{cases}\end{cases} \tag{13}$$

Here, α is set to 100 and φ_1 will thus be defined to make $\partial f/\partial\varphi$ continuous at φ_1.

3 NUMERICS

3.1 Comparison to RVE

To illustrate the applicability of the weighted potential methodology, it is implemented in to an explicit FORTRAN user element subroutine in Abaqus Explicit 6.9 (VUEL). This interphase element is referenced as the VUEL hereafter, see Fig. 8.

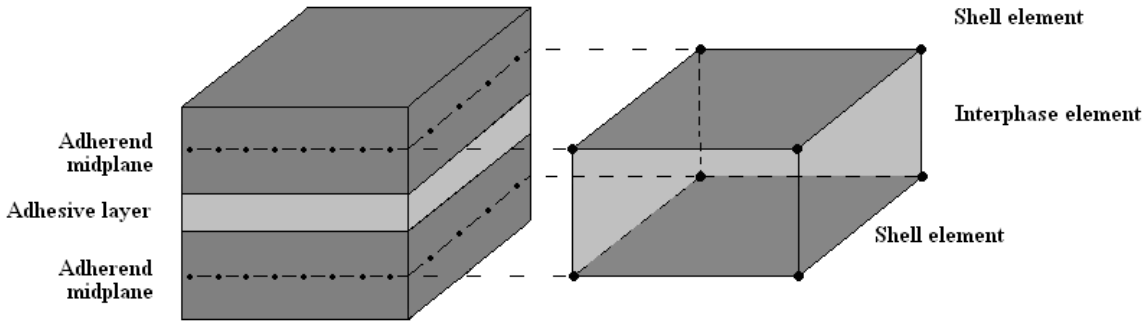

Figure 8. The VUEL interphase element connecting two shells.

Due to the lack of mixed-mode experimental data, a representative volume element is used as an experimental reference for mixed-mode experiments. The RVE consists of continuum elements coupled at every continuum element edge by cohesive elements to enable crack propagation, cf. Salomonsson and Andersson (2008). The continuum elements are allowed to deform plastically during loading. The parameters of the RVE have been calibrated to results obtained from pure mode experiments. The VUEL is loaded by controlled displacements to mimic the mixed-mode conditions of the RVE presented in Salomonsson (2008). Figure 9 illustrates a cracked RVE model.

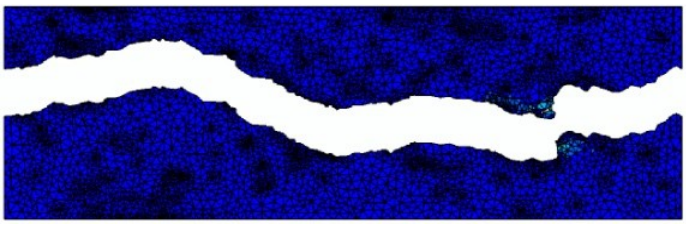

Figure 9. A cracked RVE model.

In general, mixed-mode experiments have a tendency to change the mode-mixity throughout the deformation process. Therefore, the virtual mixed-mode experiments on the RVE in Salomonsson (2008), are performed with maintained mode-mix throughout the entire deformation process. The displacements are controlled as to give mode-mixities between 0˚ (pure mode-I) and 90˚ (pure mode-II) with 15˚ intervals. Though the constraints generate non-existing forces on the RVE, the same constraints are applied to the VUEL so that a comparison of the behavior can be made. Figure 10 shows the development of equivalent plastic strain for three mode-mixities, 15˚, 45˚ and 75˚. Here, 90˚ is defined as pure mode-II.

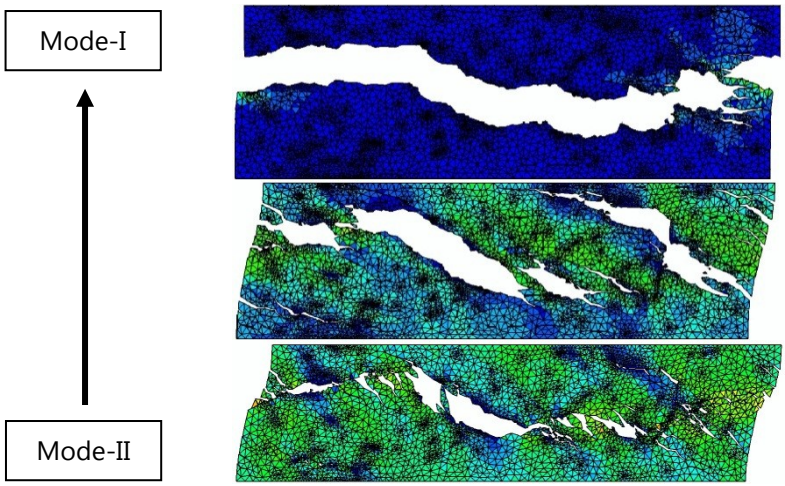

Figure 10. Equivalent plastic strain for mixed-modes 15˚, 45˚ and 75˚ for the RVE.

The only inputs to the VUEL are the pure mode results from the RVE. These results have been approximated as good as possible using trapezoidal laws for the mode-I and the mode-II results, see Fig. 11. The chosen values are given in Table 1. It can be observed that the RVE result for pure mode-II has not reached zero stress. This is due to numerical issues. Nevertheless, an assumed linear continuation of the curve has been used.

	Γ_{Ic} (J/m^2)	w_1 (μm)	w_2 (μm)	w_c (μm)	$\hat{\sigma}$ (MPa)
Mode-I	703	6	20	60	19
	Γ_{IIc} (J/m^2)	v_1 (μm)	v_2 (μm)	w_c (μm)	$\hat{\tau}$ (MPa)
Mode-II	1912	17	50	120	25

Table 1: Cohesive data for the VUEL.

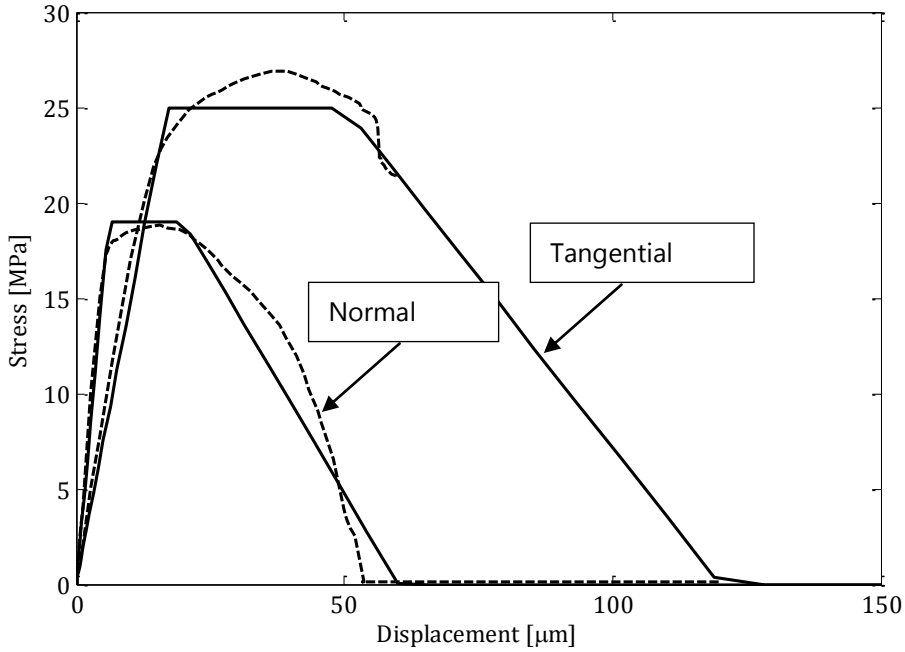

Figure 11. The approximation of pure mode behaviors for normal stress as function of relative normal separation and tangential stress as function of relative tangential separation. The RVE curves are indicated by the dashed curves and the VUEL curves are indicated by the solid curves.

The goal is to obtain the same behavior for the VUEL as for the RVE under mixed mode conditions. With the inputs shown in Fig. 11, the mixed-mode behavior is governed by the weighted potential law. Figure 12 shows the normal stresses as functions of their relative normal separations for the RVE and the VUEL for three different mode mixities, 15˚, 45˚ and 75˚. As can be seen, the behavior of the VUEL is fitted quite nicely to the RVE. For the 45˚ mode-mix, the RVE yields positive normal stress for all *w*, whilst the VUEL shows negative normal stress, or compression, for *w* exceeding 45 μm. There is a sudden drop in stress for the RVE at *w* = 45 μm where incompressibility due to plasticity have developed in the RVE, see Fig.'s 10 and 12. During this scenario, the continuum elements between the two cracks in Fig. 10 for the 45˚ mode-mix act as beams wanting to rotate. Compressive stresses arise as a consequence of the applied boundary conditions. The contact algorithm used in Salomonsson (2008), does not include non-adjacent continuum elements, but merely continuum elements initially in contact. Thus, one would expect less compressive stresses in a later stage of the deformation process since the continuum elements can overlap.

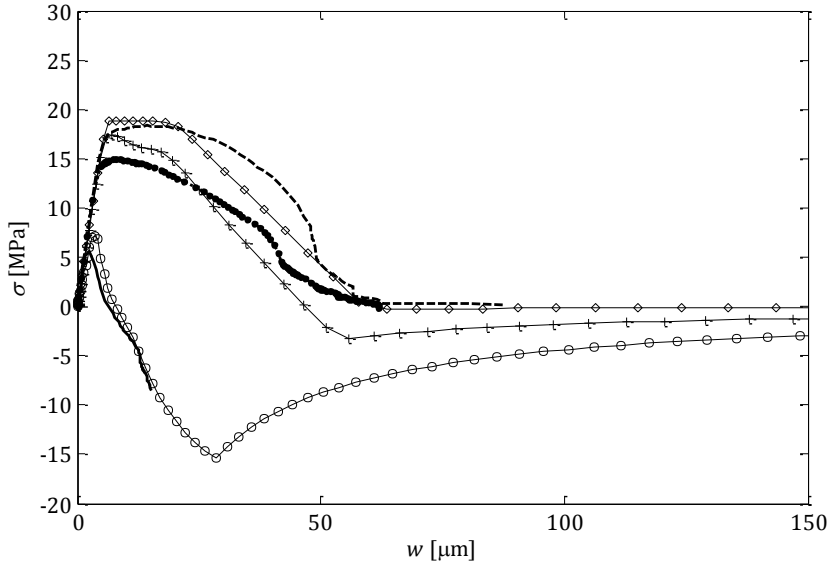

Figure 12. Comparison between the RVE and the VUEL normal stress results for mode-mixities between 15˚, 45˚ and 75˚. The RVE results are indicated by the solid (15˚), dotted (45˚) and dashed (75˚) curves. The VUEL results are indicated by the circle- (15˚), plus- (45˚) and diamond-marked (75˚) curves.

The tangential stresses as functions of their relative tangential separations for the same mode-mixities, i.e. 15˚, 45˚ and 75˚, are shown in Fig. 13 for the RVE and the VUEL. Here, the differences between the RVE and the VUEL are greater. This is not surprising considering the mismatch in Γ_c by the choice of $f(\varphi)$ according to Eq. (13). The results in Salomonsson (2008), reveal that the extrapolation used overestimates the intermediate fracture energies, i.e. $15^\circ \leq \varphi \leq 75^\circ$. It can be concluded that the overestimated energy merely affect the tangential stresses.

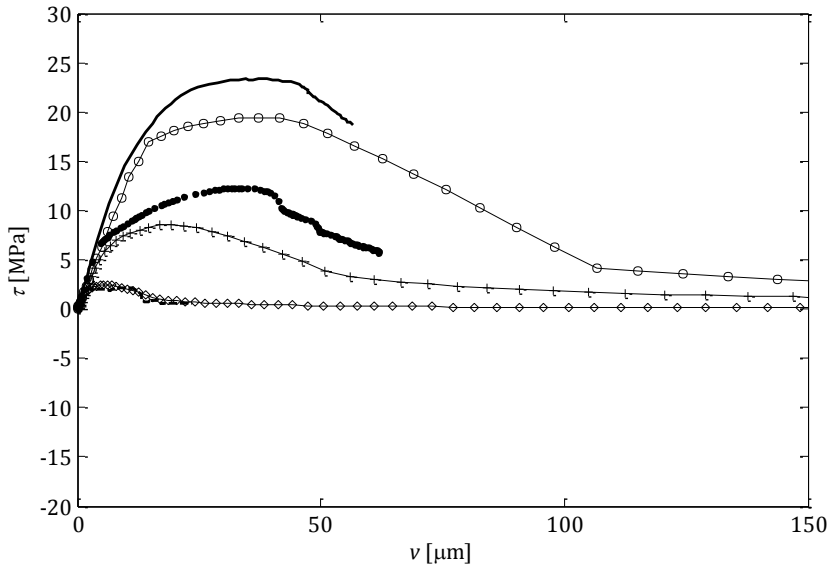

Figure 13. Comparison between the RVE and the VUEL tangential stress results for mode-mixities between 15˚, 45˚ and 75˚. The RVE results are indicated by the solid (15˚), dotted (45˚) and dashed (75˚) curves. The VUEL results are indicated by the circle- (15˚), plus- (45˚) and diamond-marked (75˚) curves.

3.2 Path dependence

In order for a cohesive law to provide a realistic physical behavior, one of its capabilities is believed to be to demonstrate path dependence. Several authors, e.g. van den Bosch et al. (2006); Park et al. (2009), argue that a cohesive law should be able to demonstrate path dependence since the dissipative mechanisms are mode dependent. As mentioned earlier, most adhesives are observed experimentally to show a fracture energy Γ_{IIc} several times larger than Γ_{Ic}. For example, in the work by Salomonsson and Andersson (2008), it is argued that for an adhesive layer subjected to pure shear the large value on Γ_{IIc} is mainly due to plasticity. On the other hand, for pure normal loading plasticity is negligible and nearly all dissipative energy is due to damage.

The VUEL is utilized herein to study path dependence. The parameters are the same as presented previously in Table 1. Before the analyses are presented some features of the cohesive law have to be clarified. The tractions for the VUEL are given by Eq.'s (8) and (9). Thus, the tractions at a specific separation (w,v) are independent of the path taken to that point. To illustrate this, the tractions in the normal and tangential direction for three different paths are compared. Path 1 is divided into two separate parts as shown in Fig. 14. In the first part, the tangential separation increases gradually until v = 80 μm whilst forcing w = 0. In the second part the normal separation gradually increase until point B is reached, keeping v fixed at 80 μm. This corresponds to a mode mixity of φ = 25˚. The loading is the reversed for path 3. Finally, for path 2 the separation in both w and v increases monotonically until point B is reached.

The normal tractions are shown in Fig. 15. For path 1, compressive stresses are observed during pure tangential loading and consequently do not contribute to the energy release rate through the first part. In the second part the stress increases, but the normal traction remain negative and does not contribute to the total energy release rate. Comparing the normal tractions between path 2 and 3 in Fig. 15, it is observed that path 2 yields significantly lower stress and as a consequence lower energy release rate.

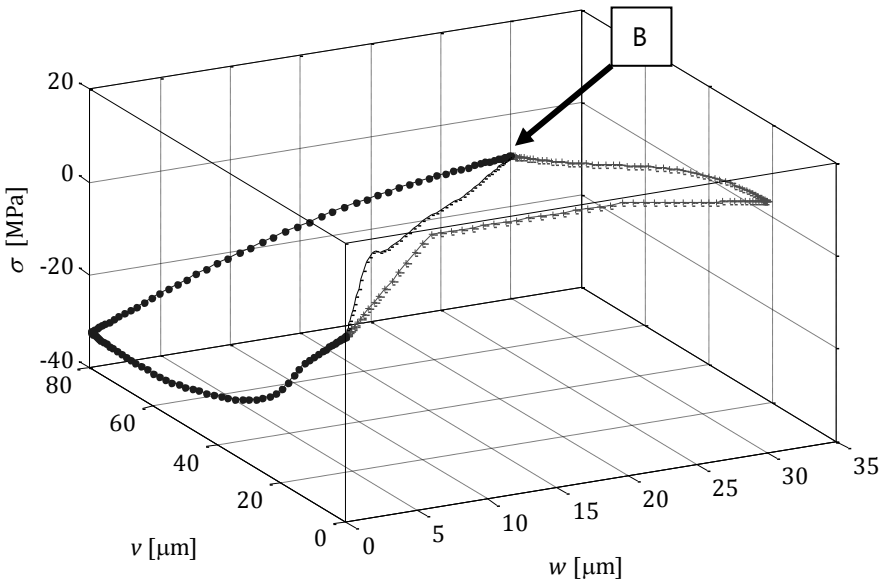

Figure 14. The normal stresses as functions of w and v for paths 1 (dotted), 2 (plus-marked) and 3 (solid). Final separation is w = 30 μm and v = 80 μm.

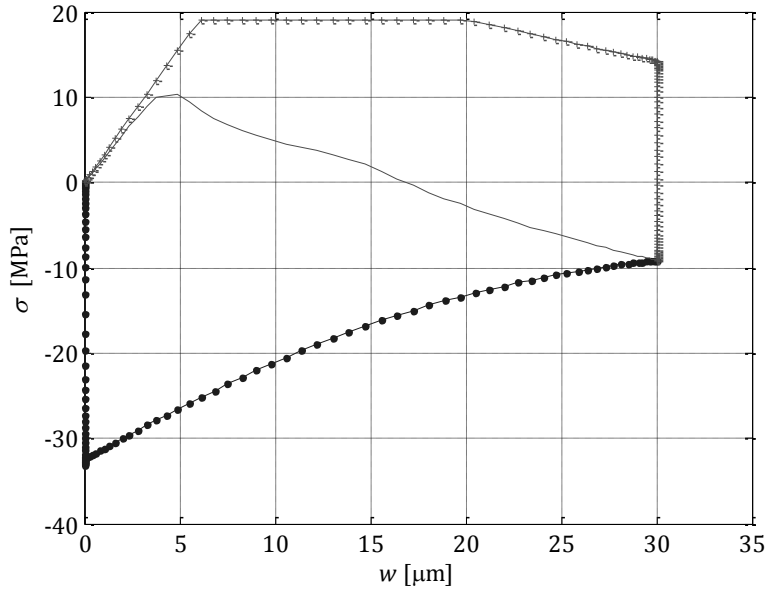

Figure 15. The normal stresses as functions of w and v for paths 1 (dotted), 2 (plus-marked) and 3 (solid). Final separation is w = 30 μm and v = 80 μm.

In Fig.'s 16 and 17 the tangential tractions are shown. For path 2 the tangential stress is considerably lower. This is due to choice of the weight function $f(\varphi)$ which, in this case, has a large gradient near $\varphi = 90^{\circ}$, see Fig 7.

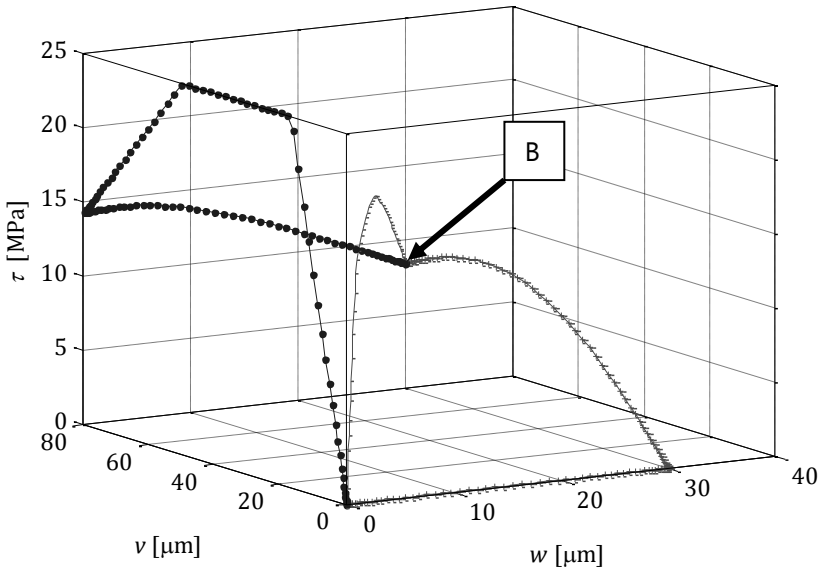

Figure 16. The tangential stresses as functions of *w* and *v* for paths 1 (dotted), 2 (plus-marked) and 3 (solid). Final separation is *w* = 30 μm and *v* = 80 μm.

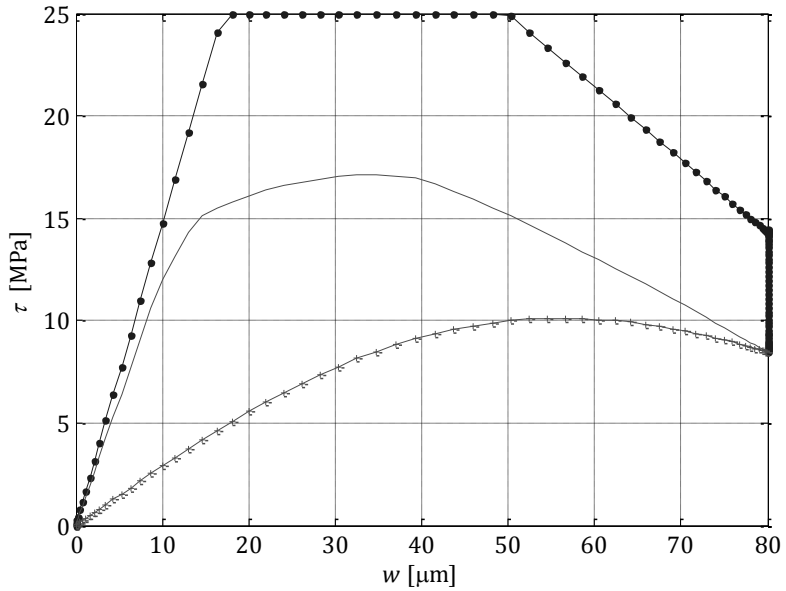

Figure 17. The tangential stresses as functions of *v* for paths 1 (dotted), 2 (plus-marked) and 3 (solid). Final separation is *w* = 30 μm and *v* = 80 μm.

The total energy release rates, i.e. the sum of the energy release rates for mode-I and mode-II, are shown in Fig. 18. The largest energy release rate is observed for Path 1. This is not surprising because of the larger value of Γ_{IIc} as compared to Γ_{Ic}. However, the energy release rate for path 2 and 3 are almost identical. This is attributed by the choice of $f(\varphi)$. The weighted potential surface in Fig. 6 does not change much for small values of φ. This indicates that the energy release rate will not change substantially in this region. Several analyses have been performed with

different choices of $f(\varphi)$. The results of the analyses support this conclusion.

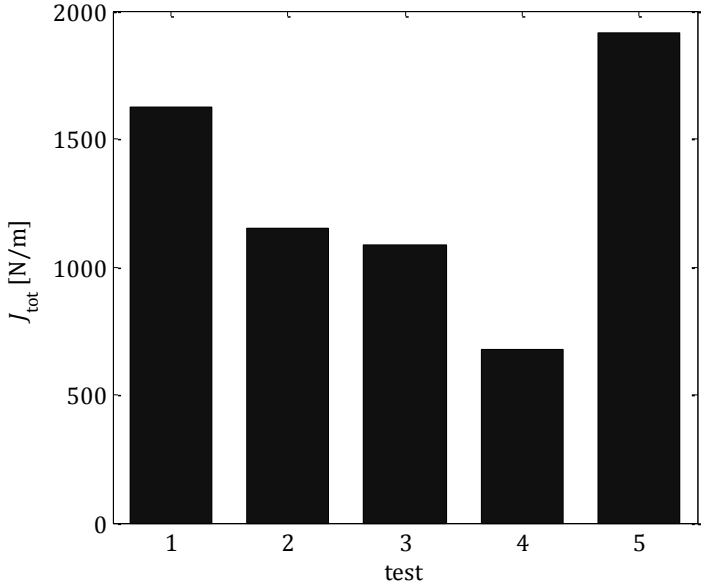

Figure 18. The total energy release rates for paths 1, 2 and 3. Tests 4 and 5 indicate the fracture energies for mode-I and mode-II, respectively.

4 CONCLUSIONS

A method to establish mixed mode behavior for adhesives from an experimental point of view has been presented. The methodology is based on pure mode experiments which can be complemented by experiments performed in mixed-mode. Through a basic fitting procedure using shape-functions, new mixed-mode data can be added to the mixed-mode cohesive law and thus increase the accuracy of the model. It can be argued that this methodology is expensive from a computational point of view. However, the experimental data is merely input to the cohesive model and does not have to be re-calculated during the computation. The comparison between the VUEL and the RVE shows the applicability of the methodology, where the rather complex epoxy adhesive material configuration is modeled by a single VUEL. The methodology is intended to be implemented in to cohesive user elements.

REFERENCES

Alfano, G., On the influence of the shape of the interface law on the application of cohesive-zone models. *Composites Science and Technology*, 66:723-730, 2006.

Alfano, G., Crisfield, M. A, Finite element models interface models for the delamination analysis of laminated composites: mechanical and computational issues. *International Journal for Numerical Methods in Engineering*, 50:1701-1736, 2001.

Alfredsson K.S., On the instantaneous energy release rate of the end-notch flexure adhesive joint specimen, *International Journal of Solids and Structures*, 41:4787–4807, 2004.

Andersson, T., Stigh, U., The stress-elongation for an adhesive layer loaded in peel using equilibrium of energetic forces. *International Journal of Solids and Structures*, 41:413-434, 2004.

Benzeggagh, M. L, Kenane, M., Measurement of mixed-mode delamination fracture toughness of unidirectional glass/epoxy composites with mixed-mode bending apparatus. *Composites Science and Technology*, 56:439-449, 1996.

De Moura, M.S.F.S., Goncalves, J.P.M., Chousal, JAG, Camphilo, R.D.S.G., Cohesive and continuum mixed-mode damage models applied to the simulation of the mechanical behavior of bonded joints. *International Journal of Adhesion & Adhesives*, 28:419-426, 2008.

Freed, Y., Banks-Sills, L., A new cohesive zone model for mixed mode interface fracture in biomaterials. Engineering Fracture Mechanics 75, 4583-4593, 2008.

Högberg, J.L., Mixed mode cohesive law. *International Journal of Fracture*, 141:549-559, 2006.

Högberg, J.L., Sørensen, B.F., Stigh, U. Constitutive behaviour of mixed mode loaded adhesive layer. *International Journal of Solids and Structures*, 44:8335–8354, 2007.

Klarbring, A., Derivation of a model of adhesively bonded joints by the asymptotic expansion method. *International Journal of Engineering Science*, 29:493–512, 1991.

Lundsgaard-Larsen, C. Sørensen, B. F, Berggren, C., Østergaard, R. C. A modified DCB specimen for measuring mixed-mode cohesive laws. *Engineering Fracture Mechanics*, 75:2514-2530, 2008.

Park, K., Paulino, g. H., Roesler, j. R., A unified potential-based cohesive model of mixed-mode fracture. *Journal of the Mechanics and Physics of Solids*, 57:891-908, 2009.

Salomonsson, K., Mixed mode modeling of a thin adhesive layer using a meso-mechanical model. *Mechanics of Materials*, 40:665-672, 2008.

Salomonsson, K., Andersson, T., Modeling and parameter calibration of an adhesive layer at the meso level. *Mechanics of Materials*, 40:48-65, 2008.

Sørensen, B. F Jørgensen, K., Jacobsen, T. K., Østergaard, R. C. DCB-specimen loaded with uneven bending moments. *International Journal of Fracture*, 141:163–176,

2006.

Sørensen, B. F., Jacobsen, T. K., Determination of cohesive laws by the J integral approach. *Engineering Fracture Mechanics*, 70:1841-1858, 2003.

Tvergaard, V., Hutchinson, J. W., The relation between crack growth resistance and fracture process parameters in elastic-plastic solids. *Journal of the Mechanics and Physics of Solids*, 40:1377-1397, 1992.

van den Bosch, M.J., Schreurs, P.J.G., Geers, M.G.D., An improved description of the exponential Xu and Needleman cohesive zone law for mixed-mode decohesion. *Engineering Fracture Mechanics*, 73:1220-1234, 2006.

Volokh, K. Y., Comparison between cohesive zone models. *Communications in Numerical Methods in Engineering*, 20:845-856, 2004.

Xie, D., Waas, A. M., Shahwan, K. W., Schroeder, J. A., Boeman, R. G., Fracture criterion for kinking cracks in a tri-material adhesively bonded joint under mixed mode loading. *Engineering Fracture Mechanics*, 72:2487-2504, 2005.

Xu, X.P., Needleman, A., Void nucleation by inclusion debonding in a crystal matrix. *Modelling Simulation Mater. Sci. Eng.*, 1 (2):111–132, 1993.